A Sliding-Mode Position Estimation Method With Chattering Suppression for *LCL*-Equipped High-Speed Surface-Mounted PMSM Drives

Yu Yao, *Student Member, IEEE*, Yunkai Huang, Fei Peng, *Member, IEEE*, and Jianning Dong, *Member, IEEE*

***Abstract*—This article proposes a sliding-mode position estimation method for high-speed surface-mounted permanent magnet synchronous machines with *LCL* filter. The implementation of the *LCL* filter aims at smoothing the motor current and reducing the iron loss caused by the harmonic currents. First, the discrete-time model of the *LCL*-filtered motor drive system is developed. Based on the developed model, the sliding-mode observer is proposed with more robustness against the parameter variation to estimate the back EMF, which contains the information of the rotor speed and position. Because of the elimination of the capacitor voltage sensors, the augmented sliding surface is designed to achieve arbitrary pole placement with only output feedback. Besides, considering the analog-to-digital scaling error and pulsewidth modulation harmonics, a reaching law with enhanced chattering suppression ability is proposed. Compared with the conventional methods, the chattering problem is well alleviated and thus the speed estimation ripple is much reduced. Finally, the effectiveness of the proposed method, even with the mismatched parameters adopted is validated at 100 kr/min with the sampling frequency 20 kHz.**

***Index Terms*—Chattering suppression, high-speed surface-mounted permanent magnet synchronous machine (HSPMSM), *LCL* filter, rotor position, sliding-mode estimation, speed estimation ripple.**

I. Introduction

HIGH-SPEED surface-mounted permanent magnet synchronous machines (HSPMSMs) have been applied on a large scale because of their high power density and gearbox-free operation [1]. Normally, the stator inductance of the HSPMSM is small because of the high operating frequency f_e. Considering the switching losses of the power switches, the switching frequency f_s is strictly restricted. In that way, with the low inductance and the limited f_s/f_e, the current ripple will be unacceptably large and the iron losses will be dramatically increased [2]. Correspondingly, the efficiency is inevitably reduced and requirements for motor thermal dissipation are increased. To solve this problem, the *LCL* output filter is often implemented to smoothen the output current as shown in Fig. 1.

For the HSPMSM drive system equipped with the *LCL* filter, there are some problems to be solved: First, the undesirable resonance oscillation in the current loop is generated and the current control method incorporated with the active damping is necessary; second, the position sensors are not suitable due to the limited mechanical strength and the reduced reliability. Therefore, the position sensorless drive is preferred. By reviewing the existing literature, various current control methods with active damping have been proposed for the *LCL*-filtered system, especially in the applications of the grid-connected converter (GCC) [3]. But there are few types of research on the position sensorless drive method for the HSPMSM equipped with *LCL* filter, especially when the capacitor voltage and the motor current are not sampled at the same time.

Conventionally, the position estimation depends on the detection of the back electromotive force (EMF) for the HSPMSM drive system. Most of these back EMF estimation methods are developed based on the continuous-time model [4]–[6]. The effectiveness of these methods will be ensured only when f_s is adequately high compared with the f_e. However, for the position sensorless drive of the HSPMSM, the f_s/f_e is relatively low due to the limited switching frequency. In this case, when an observer based on a continuous-time model is digitally implemented, the stability cannot still hold. To solve the problem caused by the discretization, the discrete-time observer design based on a fully discretized model is required [7]–[9]. The effectiveness of these methods is based on the sampling of both the ac-side capacitor voltage and the motor current. However, in the *LCL*-filtered system, the sensors of the ac-side capacitor voltage or the motor current are often eliminated to reduce cost and system complexity. Thus, these methods are no longer effective.

Several state estimation methods have been proposed for an *LCL*-filtered system to reduce the number of sensors. Kukkola and Hinkkanen [10] proposed a state observer to estimate the grid current and ac-side capacitor voltage with the converter current and grid voltage sampled for the three-phase GCC. Wang *et al.* [11] design an extended-state observer with only the converter current sampled for a single-phase GCC. And Hsu *et al.*

Manuscript received January 24, 2021; revised June 6, 2021; accepted August 25, 2021. Date of publication August 30, 2021; date of current version October 15, 2021. This work was supported in part by the National Natural Science Foundation of China under Grants 51777034 and 51707037 and in part by the Excellence Project Funds of Southeast University. Recommended for publication by Associate Editor R. Kennel. *(Corresponding author: Yunkai Huang.)*

Yu Yao, Yunkai Huang, and Fei Peng are with the School of Electrical Engineering, Southeast University, Nanjing 210096, China (e-mail: yuyao@seu.edu.cn; huangyk@seu.edu.cn; pengfei@seu.edu.cn).

Jianning Dong is with the Delft University of Technology, 2628 Delft, The Netherlands (e-mail: J.Dong-4@tudelft.nl).

Color versions of one or more figures in this article are available at https://doi.org/10.1109/TPEL.2021.3108389.

Digital Object Identifier 10.1109/TPEL.2021.3108389

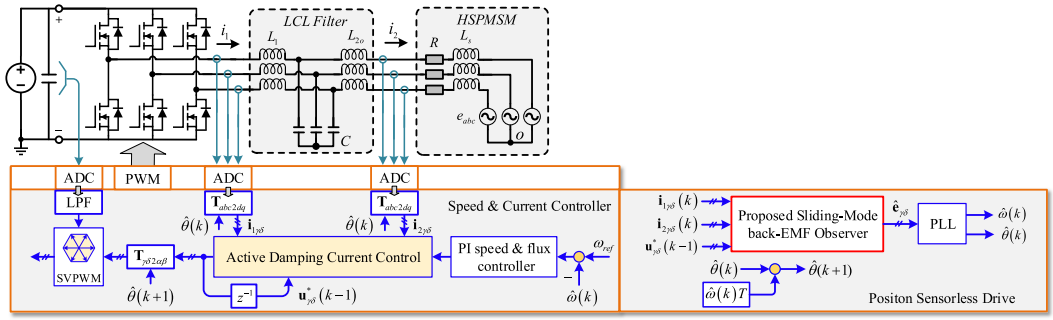

Fig. 1. Overall control diagram of the HSPMSM drive with *LCL* output filter.

[12] propose a dual observer to estimate the ac-side capacitor voltage and the motor current. But these methods are based on the continuous-time model. For the low f_s/f_e application of the HSPMSM, the discretization error will result in the estimation error and the possibility of system instability. Some estimation methods are based on the discrete-time model. The method in [10] is improved by direct discrete-time design in [13]. In [14], the ac-side capacitor voltage, the grid current, and the grid voltage are estimated by a reduced-order state observer with only the converter current sampled for a single-phase GCC. Besides, in [15], a reduced-order state observer is designed to estimate the ac-side capacitor voltage and the back EMFs for the HSPMSM with *LCL* filter. Among these methods, a full-order or reduced-order state observer is used because of the simplification. But the system uncertainties, such as mismatched parameters and the external disturbance are not considered.

The sliding-mode method is well-known for the ability to deal with the system uncertainty, but the undesirable chattering problem exists because of the discontinuous term [16]. To reduce the chattering, the time-delay estimator is widely used to compensate for the unknown disturbance and decrease the discontinuous term [17], [18]. But this method works well only for the smooth and slowly varying disturbance. For the high-frequency disturbance, the effectiveness will not be guaranteed. In the applications of the HSPMSM drive with *LCL* filter, considering the inevitable analog-to-digital converter (ADC) measurement error [19] and PWM harmonics, the high-frequency disturbance occurs and it deteriorates the chattering problem. Few types of research are involved in solving this problem.

In this article, a sliding-mode position estimation method for the HSPMSM with *LCL* filter is proposed. The estimation structure consists of the proposed sliding-mode back EMF observer and a third-order phased-locked loop (PLL). This article will focus on the design and analysis of the sliding-mode back EMF observer. Some significant improvements are achieved as follows.

1) A sliding-mode back EMF observer is designed to enhance robustness against the parameter variation.
2) An optimized reaching law with the EMF adaption law and periodic-disturbance suppression method is proposed to achieve reduced chattering and speed estimation ripple compared with the reaching law in [17].

Finally, the effectiveness of the proposed sliding-mode observer is validated with the test motor driven up to 100 kr/min.

II. Discrete-Time State-Space Modeling of HSPMSM With *LCL* Filter

Fig. 1 shows the overall control diagram of the HSPMSM drive equipped with an *LCL* output filter. The continuous-time model of the system in the stationary $\alpha\beta$ reference frame could be expressed as follows:

$$\frac{d}{dt}\mathbf{x}_s(t) = \mathbf{A}_s\mathbf{x}_s(t) + \mathbf{B}_s\mathbf{u}_s(t) \tag{1}$$

with

$$\mathbf{x}_s = [\underbrace{u_{c\alpha}\ \ u_{c\beta}}_{\mathbf{u}_{cs}}\ \ \underbrace{i_{1\alpha}\ \ i_{1\beta}}_{\mathbf{i}_{1\,s}}\ \ \underbrace{i_{2\alpha}\ \ i_{2\beta}}_{\mathbf{i}_{2\,s}}\ \ \underbrace{e_\alpha\ \ e_\beta}_{\mathbf{e}_s}]^T$$

$$\mathbf{A}_s = \begin{bmatrix} \mathbf{0} & -\frac{1}{C}\mathbf{I} & \frac{1}{C_1}\mathbf{I} & \mathbf{0} \\ -\frac{1}{L_1}\mathbf{I} & \mathbf{0} & \mathbf{0} & \mathbf{0} \\ \frac{1}{L_2}\mathbf{I} & \mathbf{0} & -\frac{R}{L_2}\mathbf{I} & -\frac{1}{L_2}\mathbf{I} \\ \mathbf{0} & \mathbf{0} & \mathbf{0} & \omega\mathbf{J} \end{bmatrix} \in \mathbf{R}^{8\times 8}$$

$$\mathbf{B}_s = [\mathbf{0}\ \ \frac{1}{L_1}\mathbf{I}\ \ \mathbf{0}\ \ \mathbf{0}]^T \in \mathbf{R}^{8\times 2} \quad \mathbf{u}_s = [u_\alpha\ \ u_\beta]^T \tag{2}$$

and

$$\mathbf{I} = \begin{bmatrix} 1 & 0 \\ 0 & 1 \end{bmatrix} \quad \mathbf{J} = \begin{bmatrix} 0 & -1 \\ 1 & 0 \end{bmatrix} \tag{3}$$

where $\mathbf{u}_s$ is the inverter output voltage, $\mathbf{u}_{cs}$ denotes the ac-side capacitor voltage, $\mathbf{i}_{1\,s}$ refers to the output current of the VSI, $\mathbf{i}_{2\,s}$ is the winding current of the motor, and $\mathbf{e}_s$ denotes the back EMF. R is the winding resistance. L_1 is the inverter-side inductance. L_{2o} is the motor-side inductance of the filter. L_s is the stator inductance. Let $L_2 = L_{2o} + L_s$. C_1 is the capacitor of the filter. ω is defined as the rotor electrical angular speed.

Assuming that the angular speed varies slowly between kT and $(k+1)T$, ω can be treated as a constant. By applying the zero-order hold method, the continuous-time state-space model in the stationary $\alpha\beta$ reference frame can be

discretized to

$$\mathbf{x}_s(k+1) = \mathbf{G}_s\mathbf{x}_s(k) + \mathbf{H}_s\mathbf{u}_s(k)$$
$$\mathbf{y}_s(k) = [\mathbf{i}_{1\,s}(k)\ \mathbf{i}_{2\,s}(k)]^T \tag{4}$$

with

$$\mathbf{G}_s = e^{\mathbf{A}_s T} \quad \mathbf{H}_s = \int_0^T e^{\mathbf{A}_s t}dt\ \mathbf{B}_s$$

where T is the sampling period.

Based on the coordinate transformation, the discrete-time model in the estimated synchronous reference frame (i.e., $\gamma\delta$ coordinate) is derived as

$$\mathbf{x}(k+1) = \mathbf{G}\mathbf{x}(k) + \mathbf{H}\mathbf{u}_{\gamma\delta}(k) + \mathbf{F}\mathbf{e}_{\gamma\delta}(k)$$
$$\mathbf{y}(k) = [\mathbf{i}_{1\gamma\delta}(k)\ \ \mathbf{i}_{2\gamma\delta}(k)]^T \tag{5}$$

with

$$\mathbf{x}(k) = [\underbrace{u_{c\gamma}\ u_{c\delta}}_{\mathbf{u}_{c\gamma\delta}}\ \underbrace{i_{1\gamma}\ i_{1\delta}}_{\mathbf{i}_{1\gamma\delta}}\ \underbrace{i_{2\gamma}\ i_{2\delta}}_{\mathbf{i}_{2\gamma\delta}}]^T$$
$$\mathbf{u}_{\gamma\delta}(k) = [u_\gamma\ u_\delta]^T \tag{6}$$

and the coefficient matrices $\mathbf{G}$, $\mathbf{H}$, and $\mathbf{F}$ can be obtained with appropriate dimensions as

$$\mathbf{G} = e^{-\mathbf{J}\omega T}\mathbf{G}_s(1:6, 1:6)$$
$$\mathbf{H} = e^{-\mathbf{J}\omega T}\mathbf{H}_s(1:6, 1:2)$$
$$\mathbf{F} = e^{-\mathbf{J}\omega T}\mathbf{G}_s(1:6, 7:8) \tag{7}$$

where the matrix exponential $e^{\mathbf{M}}$ is calculated by using inverse Laplace transform as

$$e^{\mathbf{M}} = \mathscr{L}^{-1}\{(s\mathbf{I} - \mathbf{M})^{-1}\}. \tag{8}$$

III. Overall Control Structure and the Sliding-Mode Back EMF Observer

A. Overall Control Structure

As shown in Fig. 1, the inverter current and the motor current are measured. The overall control structure consists of the active damping current control and the position sensorless drive. Because of the current control is not of concern in this article, a conventional virtual-resistance based current control method is adopted [20]. For the position sensorless drive, the back EMF is regarded as the disturbance item of the drive system. The position estimation works as a disturbance observer and exacts the information of the speed and rotor position from the estimated back EMF by a phase-locked loop.

B. Back EMF Sliding-Mode Observer

Based on the developed discrete-time model (5), the proposed sliding-mode observer is designed as

$$\hat{\mathbf{x}}(k+1) = \mathbf{G}\hat{\mathbf{x}}(k) + \mathbf{H}\mathbf{u}_{\gamma\delta}(k) + \mathbf{F}\mathbf{w}_{\gamma\delta}(k) \tag{9}$$

with

$$\hat{\mathbf{x}}(k) = [\underbrace{\hat{u}_{c\gamma}\ \hat{u}_{c\delta}}_{\hat{\mathbf{u}}_{c\gamma\delta}}\ \underbrace{\hat{i}_{1\gamma}\ \hat{i}_{1\delta}}_{\hat{\mathbf{i}}_{1\gamma\delta}}\ \underbrace{\hat{i}_{2\gamma}\ \hat{i}_{2\delta}}_{\hat{\mathbf{i}}_{2\gamma\delta}}]^T \qquad \hat{\mathbf{e}}_{\gamma\delta} = [\hat{e}_\gamma\ \hat{e}_\delta]^T \tag{10}$$

where the $\hat{\mathbf{x}}(k)$ denotes the estimated state vector. $\mathbf{w}_{\gamma\delta}(k)$ is the attraction function to converge the estimation error to zero. It should be noted that the system parameters are regarded as accurate. The robustness against the parameter variation is discussed in the later section.

Subtracting (5) from (9), the error dynamic can be obtained as

$$\tilde{\mathbf{x}}(k+1) = \mathbf{G}\tilde{\mathbf{x}}(k) + \mathbf{F}(\mathbf{w}_{\gamma\delta}(k) - \mathbf{e}_{\gamma\delta}(k)) \tag{11}$$

with

$$\tilde{\mathbf{x}}(k) = [\underbrace{\tilde{u}_{c\gamma}\ \tilde{u}_{c\delta}}_{\tilde{\mathbf{u}}_{c\gamma\delta}}\ \underbrace{\tilde{i}_{1\gamma}\ \tilde{i}_{1\delta}}_{\tilde{\mathbf{i}}_{1\gamma\delta}}\ \underbrace{\tilde{i}_{2\gamma}\ \tilde{i}_{2\delta}}_{\tilde{\mathbf{i}}_{2\gamma\delta}}]^T \tag{12}$$

where the $\tilde{\mathbf{x}}(k) = \hat{\mathbf{x}}(k) - \mathbf{x}(k)$ denotes the estimation error vector. Clearly, because the capacitor voltage are not measured, the state $\tilde{\mathbf{u}}_{c\gamma\delta}$ is not available during the design process. To converge the estimation error to zero, the discrete-time sliding surface and the reaching law are designed to guarantee the stability of the proposed back EMF observer.

C. Canonical Form

For the sliding-mode observer design of the multi-input-multi-output system, the dynamic of the sliding mode could be easily described when the model is converted into the canonical form [16]. In the proposed sliding-mode observer, the canonical form of (11) can be obtained as

$$\begin{bmatrix}\mathbf{x_u(k+1)}\\ \mathbf{y}_1(k+1)\\ \mathbf{y}_2(k+1)\end{bmatrix} = \underbrace{\begin{bmatrix}\mathbf{G}_{11} & \mathbf{G}_{12} & \mathbf{G}_{13}\\ \mathbf{G}_{21} & \mathbf{G}_{22} & \mathbf{G}_{23}\\ \mathbf{G}_{31} & \mathbf{G}_{32} & \mathbf{G}_{33}\end{bmatrix}}_{\mathbf{T}_r\mathbf{G}\mathbf{T}_r^{-1}} \underbrace{\begin{bmatrix}\mathbf{x_u(k)}\\ \mathbf{y}_1(k)\\ \mathbf{y}_2(k)\end{bmatrix}}_{\mathbf{T}_r\tilde{\mathbf{x}}}$$
$$+ \underbrace{\begin{bmatrix}\mathbf{0}\\ \mathbf{0}\\ \mathbf{B}\end{bmatrix}}_{\mathbf{T}_r\mathbf{F}} (\mathbf{w}_{\gamma\delta}(k) - \mathbf{e}_{\gamma\delta}(k)) \tag{13}$$

$$\mathbf{T}_r = \begin{bmatrix}\mathbf{I} & -\mathbf{F}_1(\mathbf{F}_2^T\mathbf{F}_2)^{-1}\mathbf{F}_2^T\\ \mathbf{0} & \mathbf{F}_t\end{bmatrix} \in \mathbf{R}^{6\times 6}$$

$$\begin{bmatrix}\mathbf{F_1^{2\times 2}} & \mathbf{F}_2^{4\times 2}\end{bmatrix}^T = \mathbf{F} \tag{14}$$

where $\mathbf{T}_r$ is the linear transformation matrix. $\mathbf{x}_u$, $\mathbf{y}_1$, and $\mathbf{y}_2$ $\in \mathbf{R}^{2\times 1}$ are the new states of the canonical form. In this article, the new system will be used for the design of the sliding-mode observer. $\mathbf{F}_2^T$ denotes the transpose of the $\mathbf{F}_2$. It should be noted that the $\mathbf{x}_u$ is also unavailable because the capacitor voltages are not measured. $\mathbf{y}_1$ and $\mathbf{y}_2$ are still available states by the linear transformation. $\mathbf{B} \in \mathbf{R}^{2\times 2}$ and is invertible. Besides, matrix $\mathbf{T}_t$ can be calculated as

$$\begin{bmatrix}\mathbf{F_t} & \mathbf{F}_p\end{bmatrix} = qr(\mathbf{F}_2) \quad \mathbf{F}_t = flipud(\mathbf{F}_t^T) \tag{15}$$

where qr denotes the QR decomposition method and $flipud$ returns a matrix with its rows flipped in the up–down direction, which both functions can be found in MATLAB.

IV. Discrete-Time Sliding Surface Design

In this section, the discrete-time surface of the proposed sliding-mode observer is designed and the arbitrary pole assignment is achieved even without the capacitor voltage measured. Besides, the general design proceeding of the sliding surface is provided.

A. Sliding Surface Design

Because of the unavailable state $\mathbf{x}_u(k)$, the poles of the traditional sliding surface can not be assigned arbitrarily with only output feedback [16]. Aiming at fixing the poles with arbitrary positions, an augmented state vector is introduced as

$$\mathbf{x}_c(k+1) = \mathbf{H}\mathbf{x}_c(k) + \mathbf{D}_1\mathbf{y}_1(k) + \mathbf{D}_2\mathbf{y}_2(k) \tag{16}$$

where $\mathbf{x}_c \in \mathbf{R}^{2\times 1}$. $\mathbf{H}$, $\mathbf{D}_1$, and $\mathbf{D}_2 \in \mathbf{R}^{2\times 2}$. Combing (13) and (16), the augmented observer system is derived as

$$\begin{bmatrix} \mathbf{x_c(k+1)} \\ \mathbf{x}_u(k+1) \\ \mathbf{y}_1(k+1) \\ \mathbf{y}_2(k+1) \end{bmatrix} = \underbrace{\begin{bmatrix} \mathbf{H} & \mathbf{0} & \mathbf{D}_1 & \mathbf{D}_2 \\ \mathbf{0} & \mathbf{G}_{11} & \mathbf{G}_{12} & \mathbf{G}_{13} \\ \mathbf{0} & \mathbf{G}_{21} & \mathbf{G}_{22} & \mathbf{G}_{23} \\ \mathbf{0} & \mathbf{G}_{31} & \mathbf{G}_{32} & \mathbf{G}_{33} \end{bmatrix}}_{\mathbf{G}_r} \underbrace{\begin{bmatrix} \mathbf{x_c(k)} \\ \mathbf{x}_u(k) \\ \mathbf{y}_1(k) \\ \mathbf{y}_2(k) \end{bmatrix}}_{\mathbf{x}_r} + \underbrace{\begin{bmatrix} \mathbf{0} \\ \mathbf{0} \\ \mathbf{0} \\ \mathbf{B} \end{bmatrix}}_{\mathbf{F}_r} (\mathbf{w}_{\gamma\delta}(k) - \mathbf{e}_{\gamma\delta}(k)). \tag{17}$$

Define the switching function as

$$\mathbf{s}(k) = \mathbf{\Gamma}_c\mathbf{x}_c(k) + \mathbf{\Gamma}_1\mathbf{y}_1(k) + \mathbf{\Gamma}_2\mathbf{y}_2(k) \in \mathbf{R}^{2\times 2} \tag{18}$$

where $\mathbf{\Gamma}_2$ is invertible and $\mathbf{\Gamma}_2^{-1} = \mathbf{B}$. In the sliding motion, $\mathbf{s}(k) = \mathbf{0}$ holds and there is

$$\mathbf{y}_2(k) = -\mathbf{M}_c\mathbf{x}_c(k) - \mathbf{M}_y\mathbf{y}_1(k) \tag{19}$$

where $\mathbf{M}_c = \mathbf{\Gamma}_2^{-1}\mathbf{\Gamma}_c$ and $\mathbf{M}_y = \mathbf{\Gamma}_2^{-1}\mathbf{\Gamma}_1$. According to (19) and (17), the dynamic of the sliding mode of the augmented system can be written as

$$\begin{bmatrix} \mathbf{x_c(k+1)} \\ \mathbf{x}_u(k+1) \\ \mathbf{y}_1(k+1) \end{bmatrix} = \underbrace{\begin{bmatrix} \mathbf{H} - \mathbf{D_2}\mathbf{M_c} & \mathbf{0} & \mathbf{D}_1 - \mathbf{D}_2\mathbf{M}_y \\ -\mathbf{G}_{13}\mathbf{M}_c & \mathbf{G}_{11} & \mathbf{G}_{12} - \mathbf{G}_{13}\mathbf{M}_y \\ -\mathbf{G}_{23}\mathbf{M}_c & \mathbf{G}_{21} & \mathbf{G}_{22} - \mathbf{G}_{23}\mathbf{M}_y \end{bmatrix}}_{\mathbf{G}_{sm}} \times \underbrace{\begin{bmatrix} \mathbf{x_c(k)} \\ \mathbf{x}_u(k) \\ \mathbf{y}_1(k) \end{bmatrix}}_{\mathbf{x}_{sm}}. \tag{20}$$

For the predefined sliding surface, the stability and the dynamic performance can be guaranteed by the pole assignment. The following proposition demonstrates that the pole positions are arbitrary by the proper selection of these matrices $\mathbf{M}_y$, $\mathbf{M}_c$, $\mathbf{H}$, $\mathbf{D}_1$, and $\mathbf{D}_2$.

Proposition: For the dynamic response of sliding mode as shown in (20), the poles of the $\mathbf{G}_{sm}$ can be arbitrary assigned by the selection as

$$\begin{aligned} \mathbf{M_y} &= \mathbf{K}_2 - \mathbf{K}_1\mathbf{L} \quad \mathbf{M}_c = \mathbf{K}_1 \\ \mathbf{H} &= \mathbf{G}_{11} + \mathbf{L}\mathbf{G}_{21} \\ \mathbf{D}_1 &= \mathbf{G}_{12} + \mathbf{L}\mathbf{G}_{22} - (\mathbf{G}_{11} + \mathbf{L}\mathbf{G}_{21})\mathbf{L} \\ \mathbf{D}_2 &= \mathbf{G}_{13} + \mathbf{L}\mathbf{G}_{23} \end{aligned} \tag{21}$$

where $\mathbf{K}_1$ and $\mathbf{K}_2$ are the gain matrices.

Proof: A new system is defined as

$$\begin{aligned} \begin{bmatrix} \mathbf{x_u(k+1)} \\ \mathbf{y}_1(k+1) \end{bmatrix} &= \begin{bmatrix} \mathbf{G_{11}} & \mathbf{G}_{12} \\ \mathbf{G}_{21} & \mathbf{G}_{22} \end{bmatrix} \begin{bmatrix} \mathbf{x_u(k)} \\ \mathbf{y}_1(k) \end{bmatrix} + \begin{bmatrix} \mathbf{G_{13}} \\ \mathbf{G}_{23} \end{bmatrix} \tilde{\mathbf{u}}(k) \\ \tilde{\mathbf{y}}(k) &= \mathbf{y}_1(k) \end{aligned} \tag{22}$$

and a reduced-order observer can be established to estimate the $\mathbf{x}_u(k)$ as

$$\begin{aligned} \mathbf{z}(k) &= (\mathbf{G}_{11} + \mathbf{L}\mathbf{G}_{21})\mathbf{z}(k) \\ &\quad + [\mathbf{G}_{12} + \mathbf{L}\mathbf{G}_{22} - (\mathbf{G}_{11} + \mathbf{L}\mathbf{G}_{21})\mathbf{L}]\,\mathbf{y}_1(k) \\ &\quad + (\mathbf{G}_{13} + \mathbf{L}\mathbf{G}_{23})\tilde{\mathbf{u}}(k) \\ \mathbf{z}(k) &= \hat{\mathbf{x}}_u(k) + \mathbf{L}\mathbf{y}_1(k) \end{aligned} \tag{23}$$

where $\hat{\mathbf{x}}_u$ is the estimated value of the $\mathbf{x}_u(k)$ and $\mathbf{L}$ is gain matrix so that $\mathbf{G}_{11} + \mathbf{L}\mathbf{G}_{21}$ is stable. The selection of $\mathbf{L}$ can be treated as the static state feedback problem for the system $(\mathbf{G}_{11}, -\mathbf{G}_{21})$. Clearly, the pole assignment of $\mathbf{G}_{11} + \mathbf{L}\mathbf{G}_{21}$ is arbitrary and the pole vector is defined as $\mathbf{p}_L \in \mathbf{R}^{2\times 1}$. For the system (22), a full-state feedback controller can be designed as

$$\begin{aligned} \tilde{\mathbf{u}}(k) &= -\mathbf{K}_1\hat{\mathbf{x}}_u(k) - \mathbf{K}_2\mathbf{y}_1(k) \\ &= -\mathbf{K}_1\mathbf{z}(k) - (\mathbf{K}_2 - \mathbf{K}_1\mathbf{L})\mathbf{y}_1(k) \end{aligned} \tag{24}$$

where $\mathbf{K}_1$ and $\mathbf{K}_2$ are the gain matrices and can be calculated by the full-state feedback to fix poles at any desirable positions, which is defined as $\mathbf{p}_u \in \mathbf{R}^{4\times 1}$.

According to (21), the closed-loop system formed from (22) and (23) is derived as

$$\begin{bmatrix} \mathbf{z(k+1)} \\ \mathbf{x}_u(k+1) \\ \mathbf{y}_1(k+1) \end{bmatrix} = \underbrace{\begin{bmatrix} \mathbf{H} - \mathbf{D_2}\mathbf{M_c} & \mathbf{0} & \mathbf{D}_1 - \mathbf{D}_2\mathbf{M}_y \\ -\mathbf{G}_{13}\mathbf{M}_c & \mathbf{G}_{11} & \mathbf{G}_{12} - \mathbf{G}_{13}\mathbf{M}_y \\ -\mathbf{G}_{23}\mathbf{M}_c & \mathbf{G}_{21} & \mathbf{G}_{22} - \mathbf{G}_{23}\mathbf{M}_y \end{bmatrix}}_{\mathbf{A}_c} \times \begin{bmatrix} \mathbf{z(k)} \\ \mathbf{x}_u(k) \\ \mathbf{y}_1(k) \end{bmatrix}. \tag{25}$$

It can be easily verified that the matrix $\mathbf{A}_c$ is identical to the matrix $\mathbf{G}_{sm}$, which defines the stability and the dynamic

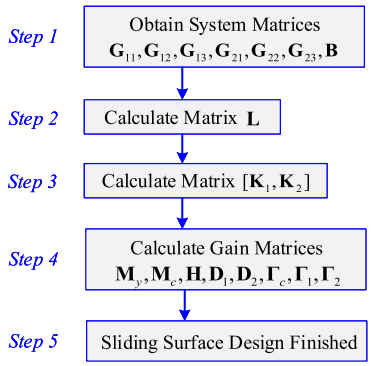

Fig. 2. Design steps of the discrete-time sliding surface.

response of the sliding surface. Additionally, from the separation principle, the closed-loop poles of $\mathbf{A}_c$ consists of the $\mathbf{p}_L$ and $\mathbf{p}_u$. Therefore, when the matrices ($\mathbf{H}$, $\mathbf{D}_1$, $\mathbf{D}_2$, $\mathbf{M}_c$, and $\mathbf{M}_y$) are selected based on (21), the poles of the designed sliding surface can be placed arbitrarily.

B. General Design Proceeding

Fig. 2 shows the design steps of the proposed discrete-time sliding surface. The detailed descriptions are demonstrated as follows.

1) *Step 1*: Based on the canonical form of the error dynamic (13), the following coefficient matrices can be obtained as:
$$\mathbf{G}_{11},\mathbf{G}_{12},\mathbf{G}_{13},\mathbf{G}_{21},\mathbf{G}_{22},\mathbf{G}_{23},\mathbf{B}\in\mathbf{R}^{2\times 2}.$$
2) *Step 2*: The gain matrix $\mathbf{L}$ is calculated by the state-feedback pole assignment of the system ($\mathbf{G}_{11}$, $-\mathbf{G}_{12}$). The desired pole vector is $\mathbf{p}_L\in\mathbf{R}^{2\times 1}$.
3) *Step 3*: The gain matrix $[\mathbf{K}_1,\mathbf{K}_2]$ is calculated by the state-feedback pole assignment of the system formed as
$$\left(\begin{bmatrix}\mathbf{G_{11}} & \mathbf{G}_{12}\\ \mathbf{G}_{21} & \mathbf{G}_{22}\end{bmatrix},\begin{bmatrix}\mathbf{G_{13}}\\ \mathbf{G}_{23}\end{bmatrix}\right).$$
The desired pole vector is $\mathbf{p}_u\in\mathbf{R}^{4\times 1}$.
4) *Step 4*: Based on (21), the following matrices can be calculated as:
$$\mathbf{M}_y,\mathbf{M}_c,\mathbf{H},\mathbf{D}_1,\mathbf{D}_2\in\mathbf{R}^{2\times 2}$$
and the coefficient matrices of the $\mathbf{s}(k)$ are derived as
$$\mathbf{\Gamma}_c=\mathbf{B}^{-1}\mathbf{M}_c\quad\mathbf{\Gamma}_1=\mathbf{B}^{-1}\mathbf{M}_y\quad\mathbf{\Gamma}_2=\mathbf{B}^{-1}.$$
5) *Step 5*: According to (16) and (18), the design of the discrete-time sliding surface is finished. The stability and the dynamic performance are guaranteed by the desired pole vector $[\mathbf{p}_L,\mathbf{p}_u]$.

It should be noted that the design contains many matrix manipulations. To achieve digital implementation easily, these math computations can be done offline and serves as lookup tables or polynomial curve fitting in the digital controller.

V. Disturbance Analysis and Chattering-Suppression Reaching Law Design

In the sliding-mode control, the reaching law is designed to guarantee the convergence to the sliding surface from any initial state, which is called the reaching mode. In this section, the disturbances considering the ADC scaling error and PWM harmonics are first discussed. Then a reaching law with the back EMF adaption and the periodic-disturbance estimator is designed to guarantee stability and alleviate the chattering problem.

A. Reaching Mode Dynamic Description

In order to simplify the design process, a linear transformation is also introduced for (17) as

$$\begin{bmatrix}\mathbf{x_c}(\mathbf{k}+\mathbf{1})\\ \mathbf{x}_u(k+1)\\ \mathbf{y}_1(k+1)\\ \mathbf{s}(k+1)\end{bmatrix}=\underbrace{\begin{bmatrix}\cdots & \cdots & \cdots & \cdots\\ \vdots & \vdots & \vdots & \vdots\\ \mathbf{G}_c & \mathbf{G}_u & \mathbf{G}_y & \mathbf{G}_s\end{bmatrix}}_{\mathbf{T}_y\mathbf{G}_r\mathbf{T}_y^{-1}}\underbrace{\begin{bmatrix}\mathbf{x_c}(\mathbf{k})\\ \mathbf{x}_u(k)\\ \mathbf{y}_1(k)\\ \mathbf{s}(k)\end{bmatrix}}_{\mathbf{T}_y\mathbf{x}_r}+\underbrace{\begin{bmatrix}\mathbf{0}\\ \mathbf{0}\\ \mathbf{0}\\ \mathbf{I}\end{bmatrix}}_{\mathbf{T}_y\mathbf{F}_r}\times(\mathbf{w}_{\gamma\delta}(k)-\mathbf{e}_{\gamma\delta}(k)) \tag{26}$$

$$\mathbf{T}_y=\begin{bmatrix}\mathbf{I} & \mathbf{0} & \mathbf{0} & \mathbf{0}\\ \mathbf{0} & \mathbf{I} & \mathbf{0} & \mathbf{0}\\ \mathbf{0} & \mathbf{0} & \mathbf{I} & \mathbf{0}\\ \mathbf{\Gamma}_c & \mathbf{0} & \mathbf{\Gamma}_1 & \mathbf{\Gamma}_2\end{bmatrix}. \tag{27}$$

Therefore, the dynamic of the reaching mode is derived as

$$\begin{aligned}\mathbf{s}(k+1)=&\mathbf{G}_s\mathbf{s}(k)+\mathbf{w}_{\gamma\delta}(k)\\&+\mathbf{G}_c\mathbf{x}_c(k)+\mathbf{G}_y\mathbf{y}_1(k)+\mathbf{G}_u\mathbf{x}_u(k)-\mathbf{e}_{\gamma\delta}(k)\end{aligned} \tag{28}$$

where the $\mathbf{G}_s$ is the system matrix and the $\mathbf{w}_{\gamma\delta}(k)$ is the system input. $\mathbf{e}_{\gamma\delta}(k)$ and $\mathbf{x}_u(k)$ could not be obtained directly because the position sensor and capacitor voltage sensor are eliminated.

In the full-digitally drive system, the disturbances of the above reaching mode are usually derived from the following.

1) ADC Scaling Error: Normally, the current signal will be transferred to the voltage signal via a shunt resistance or a current transformer. The voltage signal should be limited to the maximum input of the ADC chip. After the sampling, the sampled current can be calculated by the sampled voltage and the nominal ADC gain. However, the real ADC gain varies due to the temperature variation and nominal error of the circuit components. In that case, there exists a deviation between the real current and the calculated current in the digital controller, which is called ADC scaling error. According to [19], the ADC scaling error causes the harmonic component at the fundamental

TABLE I
FUNDAMENTAL AND HARMONIC COMPONENTS OF A SINGLE-PHASE INVERTER OUTPUT VOLTAGE. $V_0 = 60$ V, $M = 0.9$, $f_e = 1666.66$ Hz AND $f_s = 20$ kHz

Frequency (Hz)	Amplitude (V)
1666.67 (1^{st})	26.723
3333.33 (2^{nd})	0.4097
5000 (3^{rd})	0.1288
6666.67 (4^{th})	0.0073
8333.33 (5^{th})	0.0013

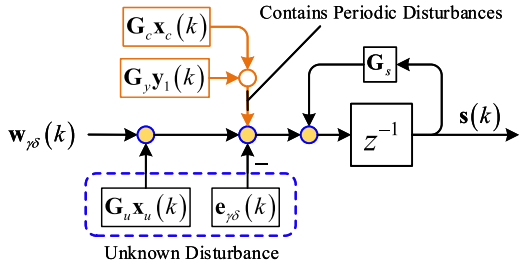

Fig. 3. Diagram of the reaching mode.

frequency (i.e., f_e) and the attenuation is insufficient in the stationary coordinate. In that case, it results in the oscillation at $2f_e$ in the sampled values after the synchronous coordinate transformation.

2) PWM Harmonics: In a digital modulation system, the regular sampled PWM strategy is widely used, where the low-frequency reference waveforms are sampled and then held constant during each carrier interval. According to [21] and [22], for a symmetrical sampling with triangular carrier (positive peak sampled), the fundamental and harmonic components of the single-phase inverter output voltage are demonstrated in Table I. The third harmonic component is eliminated because the phase angles are the same for the three-phase legs.

Therefore, the sampled values contain the second and the third harmonic components, which indicates the item $\mathbf{x}_c(k)$, $\mathbf{y}_1(k)$, and $\mathbf{x}_u(k)$ suffer from the periodic disturbances ($2f_e$ and $3f_e$), as shown in Fig. 3. In this article, the sum of the item $\mathbf{G}_c\mathbf{x}_c(k)$, $\mathbf{G}_y\mathbf{y}_1(k)$, and $\mathbf{G}_u\mathbf{x}_u(k)$ is treated as a lump periodic disturbance, which is defined as

$$\mathbf{d}(k) = \mathbf{G}_c\mathbf{x}_c(k) + \mathbf{G}_y\mathbf{y}_1(k) + \mathbf{G}_u\mathbf{x}_u(k). \tag{29}$$

Fig. 4(a) and (d) shows the waveforms and the FFT analysis of the periodic disturbance when the speed is 100 kr/min. In this way, the dynamic expression of the reaching mode can be described as

$$\mathbf{s}(k+1) = \mathbf{G}_s\mathbf{s}(k) + \mathbf{w}_{\gamma\delta}(k) + \mathbf{d}(k) - \mathbf{e}_{\gamma\delta}(k). \tag{30}$$

In the sliding-mode disturbance suppression methods, the time-delay estimation is popularly used as the following.

1) In [17], the disturbance $\mathbf{d}(k)$ can be compensated by the $\mathbf{d}(k-1)$, which is obtained by a time-delay disturbance estimator. The disturbance compensation error is

$$\tilde{\mathbf{d}}(k) = \mathbf{d}(k) - \mathbf{d}(k-1). \tag{31}$$

2) In [18], the disturbance $\mathbf{d}(k)$ is designed to be compensated by the $2\mathbf{d}(k-1) - \mathbf{d}(k-2)$. Both $\mathbf{d}(k-1)$ and $\mathbf{d}(k-2)$ are obtained by a time-delay disturbance estimator, which is the same as in [17]. Finally, the disturbance compensation error is

$$\tilde{\mathbf{d}}(k) = \mathbf{d}(k) - 2\mathbf{d}(k-1) + \mathbf{d}(k-2). \tag{32}$$

where the $\tilde{\mathbf{d}}(k)$ is the compensation error.

Fig. 4 shows the periodic disturbance $\mathbf{d}(k)$ and the compensation error $\tilde{\mathbf{d}}(k)$ by the time-delay disturbance compensation method in [17] and [18]. It can be easily observed that both the compensation errors are still large, even become worse in [18]. In that way, the undesirable chattering will deteriorate the estimation of the back EMF and thus the speed estimation suffers from the periodic disturbance, which will be validated later.

B. Chattering-Suppression Reaching Law Design

To solve the aforementioned problem, a reaching law with chattering suppression ability is proposed and the structure is shown in Fig. 5. First, a bandpass-based periodic disturbance suppression method is designed to deal with $\mathbf{d}(k)$, and then an adaption law for the back EMF is implemented to estimate the $\mathbf{e}_{\gamma\delta}$.

The optimized nonswitching reaching law of the proposed sliding-mode observer is designed as

$$\mathbf{w}_{\gamma\delta}(k) = (-\mathbf{G}_s + \mathbf{Q})\mathbf{s}(k) + \hat{\mathbf{e}}_{\gamma\delta}(k) - \hat{\mathbf{d}}(k) \tag{33}$$

and the back EMF adaption is designed as

$$\hat{\mathbf{e}}_{\gamma\delta}(k) = \hat{\mathbf{e}}_{\gamma\delta}(k-1) + k(\mathbf{s}(k) - \mathbf{Q}\mathbf{s}(k-1)) \tag{34}$$

and the bandpass-based periodic disturbance suppression is designed as

$$\hat{\mathbf{d}}(k) = G_{bp}(z)\left(z^{-N+1}\left(\mathbf{s}(k) - \mathbf{Q}\mathbf{s}(k-1)\right) + \hat{\mathbf{d}}(k-1)\right) \tag{35}$$

where $\mathbf{Q}$ is a diagonal convergent matrix with both eigenvalues (Q_1 and Q_2) inside of the unit cycle. $\hat{\mathbf{e}}_{\gamma\delta}(k)$ denotes the estimated back EMF. $\hat{\mathbf{d}}(k)$ is the periodic disturbance compensation. $G_{bp}(z)$ represents the bandpass filter, where the center frequency is located at $2f_e$ and $3f_e$. N is the ratio of the sampling/harmonic frequency.

Substituting (33) into (30), it is derived as

$$\mathbf{s}(k+1) = \mathbf{Q}\mathbf{s}(k) + \hat{\mathbf{e}}_{\gamma\delta}(k) - \mathbf{e}_{\gamma\delta}(k) - \hat{\mathbf{d}}(k) + \mathbf{d}(k) \tag{36}$$

In that case, the state of the switching function can be obtained by solving the above difference equation as

$$\mathbf{s}(k+1) = \mathbf{Q}^k\mathbf{s}(1) + \underbrace{\sum_{j=0}^{k-1}\mathbf{Q}^j(\hat{\mathbf{e}}_{\gamma\delta}(k-j) - \mathbf{e}_{\gamma\delta}(k-j))}_{O_1} + \underbrace{\sum_{j=0}^{k-1}\mathbf{Q}^j(\mathbf{d}(k-j) - \hat{\mathbf{d}}(k-j))}_{O_2}. \tag{37}$$

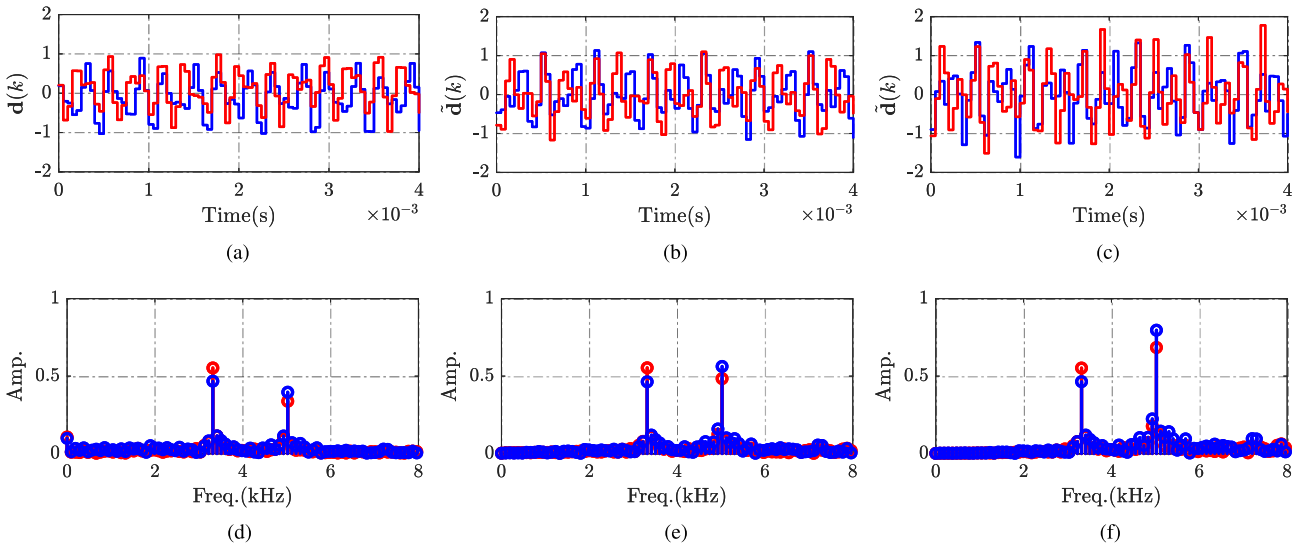

Fig. 4. Periodic disturbance $\mathbf{d}(k)$ and the compensation error $\tilde{\mathbf{d}}(k)$ by the time-delay estimator in [17] and [18]. (a) d(k). (b) Disturbance compensation error [17]. (c) Disturbance compensation error [18]. (d) FFT of d(k). (e) FFT of disturbance compensation error [17]. (f) FFT of disturbance compensation error [18].

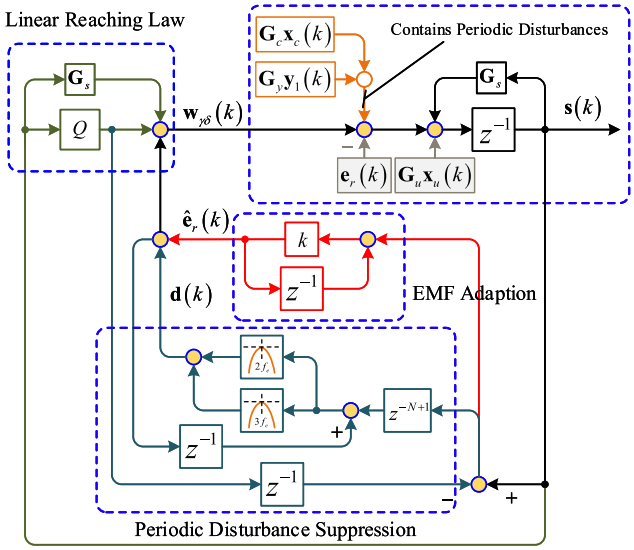

Fig. 5. Structure of the proposed chattering-suppression reaching law.

In order to ensure the convergence of the $\mathbf{s}(k)$, the O_1 and O_2 have to converge to zero.

1) EMF Adaption: The convergence of the O_1 is guaranteed by the EMF adaption law. Based on (36), there is

$$\mathbf{s}(k) = \mathbf{Q}\mathbf{s}(k-1) + \hat{\mathbf{e}}_{\gamma\delta}(k-1) - \mathbf{e}_{\gamma\delta}(k-1) - \hat{\mathbf{d}}(k-1) + \mathbf{d}(k-1). \tag{38}$$

Substituting (34) into (38), it is derived as

$$\hat{\mathbf{e}}_{\gamma\delta}(k) = \hat{\mathbf{e}}_{\gamma\delta}(k-1) + k(\mathbf{p}(k) - \hat{\mathbf{e}}_{\gamma\delta}(k-1)) \tag{39}$$

where $\mathbf{p}(k) = \mathbf{e}_{\gamma\delta}(k-1) + \mathbf{d}(k-1) - \hat{\mathbf{d}}(k-1)$. The $\hat{\mathbf{e}}_{\gamma\delta}(k)$ can be regarded as the value from the $\mathbf{p}(k)$ through a lowpass filter. For the $\mathbf{p}(k)$, the $\mathbf{d}(k-1)$ and $\hat{\mathbf{d}}(k-1)$ are composed of the second and third harmonic components, but $\mathbf{e}_{\gamma\delta}(k-1)$ is only related with the angular speed and varies slowly. Therefore, the $\mathbf{d}(k-1)$ and $\hat{\mathbf{d}}(k-1)$ can be easily filtered out and the $\hat{\mathbf{e}}_{\gamma\delta}(k)$ is equal to the $\mathbf{e}_{\gamma\delta}(k-1)$. In that case, the O_1 can be rewritten as

$$O_1 = \sum_{j=0}^{k-1} \mathbf{Q}^j(\mathbf{e}_{\gamma\delta}(k-j) - \mathbf{e}_{\gamma\delta}(k-j-1)). \tag{40}$$

Considering the $\mathbf{e}_{\gamma\delta}(k)$ is slowly varying during a sampling period, the item $\mathbf{e}_{\gamma\delta}(k-j) - \mathbf{e}_{\gamma\delta}(k-j-1)$ is considerably small and on the steady state, it will converge to zero with the attenuation of $\mathbf{Q}^j$.

2) Periodic Disturbance Suppression: Based on (36), the periodic disturbance can be calculated as

$$\mathbf{s}(k) - \mathbf{Q}\mathbf{s}(k-1) + \hat{\mathbf{d}}(k-1) = \hat{\mathbf{e}}_{\gamma\delta}(k-1) - \mathbf{e}_{\gamma\delta}(k-1) + \mathbf{d}(k-1) \tag{41}$$

and, thus, according to (35), there is

$$\hat{\mathbf{d}}(k) = G_{bp}(z)\left(\hat{\mathbf{e}}_{\gamma\delta}(k-N) - \mathbf{e}_{\gamma\delta}(k-N) + \mathbf{d}(k-N)\right). \tag{42}$$

Because both the $\hat{\mathbf{e}}_{\gamma\delta}(k-N)$ and $\mathbf{e}_{\gamma\delta}(k-N)$ are direct components

$$\hat{\mathbf{d}}(k) = G_{bp}(z)\mathbf{d}(k-N). \tag{43}$$

Considering the $\hat{\mathbf{d}}(k)$ is periodic, $\hat{\mathbf{d}}(k) = \mathbf{d}(k)$ holds. In that case, the O_2 can be rewritten as

$$O_2 = \sum_{j=0}^{k-1} \mathbf{Q}^j(\mathbf{d}(k-j) - \mathbf{d}(k-j-N)) \to 0. \tag{44}$$

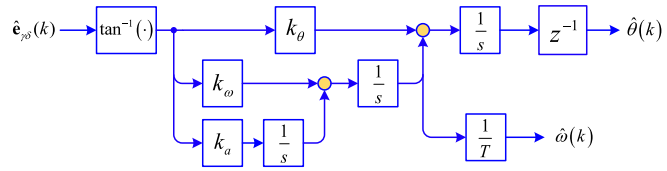

Fig. 6. PLL structure.

The transfer function of the bandpass filter is introduced as

$$G_{bp}(z) = \frac{1-a_2}{2}\frac{1-z^{-2}}{1-a_1 z^{-1}+a_2 z^{-2}} \tag{45}$$

and the coefficients are defined as

$$a_1 = \frac{2\cos(\omega_n T)}{1+\tan(\Omega T/2)} \quad a_2 = \frac{1-\tan(\Omega T/2)}{1+\tan(\Omega T/2)} \tag{46}$$

where ω_n is the center frequency and Ω is the -3 dB bandwidth.

Therefore, with the proposed reaching law, the $\mathbf{s}(k)$ is well ensured to converge to zero and the chattering problem can be well relieved with the periodic disturbance suppression method.

C. Speed and Position Estimation

With the back EMF estimation, the position error can be extracted as

$$\tilde{\theta}(k) = \tan^{-1}(-\frac{\hat{e}_\gamma(k)}{\hat{e}_\delta(k)}) \tag{47}$$

where the $\tilde{\theta}$ denotes the estimated position error. Then, a PLL is implemented to estimate the speed and the rotor position, as shown in Fig. 6. The PLL can be expressed as [23]

$$\begin{aligned}\hat{\theta}(k+1) &= \hat{\theta}(k) + \hat{\omega}(k)T + k_\theta\tilde{\theta}(k)\\ \hat{\omega}(k+1) &= \hat{\omega}(k) + \hat{a}(k)T + k_\omega\tilde{\theta}(k)\\ \hat{a}(k+1) &= \hat{a}(k) + k_a\tilde{\theta}(k)\end{aligned} \tag{48}$$

where the k_θ, k_ω, and k_a are the PLL coefficients. The corresponding transfer function from the $\tilde{\theta}$ to the estimated position $\hat{\theta}$ is derived as

$$G_{\text{PLL}} = \frac{k_\theta z^2 + (k_\omega T - 2k_\theta)z + k_\theta - k_\omega T + k_a T^2}{(z-1)^3}. \tag{49}$$

Fig. 7 shows the bode diagram of the $\mathbf{G}_{\text{PLL}}$ with the different coefficient selections. Based on the bode diagram and the classical control theory, there are following points.

1) k_θ mainly affects the 0 dB crossover frequency. The larger k_θ increases the tracking bandwidth, but the harmonic suppression capability is reduced.
2) k_ω mainly affects the gain at the middle frequency. The large k_ω will increase the tracking performance in the speed-dynamic applications.
3) k_a mainly affects the gain at the low frequency. The large k_a will reduce the steady-state tracking error.

Based on these considerations, the PLL parameters in this article are selected as

$$k_\theta = 0.1 \quad k_\omega = 10 \quad k_a = 10. \tag{50}$$

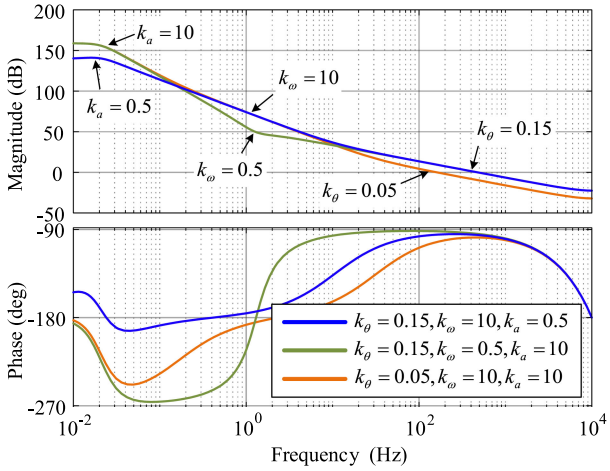

Fig. 7. Bode diagram of the PLL.

D. EMF Adaption Gain Selection

As the analysis above, the EMF adaption works as a lowpass filter and thus the adaption gain k is equivalent with the cutoff frequency. The coefficient k is adjusted to make the following equations hold.

$$k = 2f_e\sqrt{\frac{\varphi^2}{1-\varphi^2}}T \tag{51}$$

where φ is the predefined attenuation gain at $2f_e$.

VI. Parameter Variation

Considering the parameter mismatch, the proposed sliding-mode observer with mismatched parameters can be established as

$$\hat{\mathbf{x}}(k+1) = \hat{\mathbf{G}}\hat{\mathbf{x}}(k) + \hat{\mathbf{H}}\mathbf{u}_{\gamma\delta}(k) + \hat{\mathbf{F}}\mathbf{w}_{\gamma\delta}(k). \tag{52}$$

By (52) minus (5), the error dynamic can be obtained as

$$\tilde{\mathbf{x}}(k+1) = \hat{\mathbf{G}}\tilde{\mathbf{x}}(k) + \hat{\mathbf{F}}(\mathbf{w}_{\gamma\delta}(k) - \mathbf{e}_{\gamma\delta}(k)) + \boldsymbol{\xi}(k,\mathbf{x}) \tag{53}$$

and

$$\boldsymbol{\xi}(k,\mathbf{x}) = \Delta\mathbf{F}\mathbf{e}_{\gamma\delta}(k) + \Delta\mathbf{G}\mathbf{x}(k) + \Delta\mathbf{H}\mathbf{u}_{\gamma\delta}(k) \tag{54}$$

where $\hat{\mathbf{G}} = \mathbf{G} + \Delta\mathbf{G}$, $\hat{\mathbf{H}} = \mathbf{H} + \Delta\mathbf{H}$, and $\hat{\mathbf{F}} = \mathbf{F} + \Delta\mathbf{F}$. It is worthy noting that $\Delta\mathbf{F}\mathbf{e}_{\gamma\delta}(k)$, $\Delta\mathbf{G}\mathbf{x}(k)$ and $\Delta\mathbf{H}\mathbf{u}_{\gamma\delta}(k)$ are regarded as the uncertain disturbance.

After the linear transformation mentioned above, the dynamic of the reaching mode and the sliding mode can be written as

$$\begin{aligned}\mathbf{x}_{sm}(k+1) &= \hat{\mathbf{G}}_{sm}\mathbf{x}_{sm}(k) + \boldsymbol{\xi}_1(k,\mathbf{x})\\ \mathbf{s}(k+1) &= \hat{\mathbf{G}}_s\mathbf{s}(k) + \mathbf{w}_{\gamma\delta}(k) - \mathbf{e}_{\gamma\delta}(k) + \mathbf{d}(k)\\ &\quad + \boldsymbol{\xi}_2(k,\mathbf{x})\end{aligned} \tag{55}$$

where $\boldsymbol{\xi}_1(k,\mathbf{x}_{sm})$ is defined as the unmatched uncertainty and $\boldsymbol{\xi}_2(k,\mathbf{x}_{sm})$ denotes the matched uncertainty.

A. Effect on Sliding Mode

According to (55), the impact of the matched uncertainty $\boldsymbol{\xi}_2(k,\mathbf{x})$ on the sliding mode is eliminated, which is often called the invariance. But for the unmatched uncertainty $\boldsymbol{\xi}_1(k,\mathbf{x})$, it does not lie the range space of the input distribution matrix and the ideal sliding mode will no longer exist [16]. In the sliding-surface design, the $\mathbf{G}_{sm}$ is stable with all the eigenvalues located inside the unit cycle. Considering the $\boldsymbol{\xi}_1(k,\mathbf{x})$ is bounded, based on the BIBO stability, $\mathbf{x}_{sm}(k)$ is also bounded. Therefore, the stability of the sliding mode is also ensured, but the $\mathbf{x}_{sm}(k)$ may not converge to zero with the excitation of $\boldsymbol{\xi}_1(k,\mathbf{x})$.

B. Effect on Reaching Mode

Considering the parameter variation, the reaching law is modified as

$$\mathbf{w}_{\gamma\delta}(k) = (-\mathbf{G}_s + \mathbf{Q})\mathbf{s}(k) + \hat{\mathbf{e}}_{\gamma\delta}(k) - \hat{\mathbf{d}}(k) \tag{56}$$

and the dynamic of the $\mathbf{s}(k)$ is derived as

$$\begin{aligned}\mathbf{s}(k+1) = {} & \mathbf{Q}\mathbf{s}(k) + \hat{\mathbf{e}}_{\gamma\delta}(k) - \mathbf{e}_{\gamma\delta}(k) \\ & - \hat{\mathbf{d}}(k) + \mathbf{d}(k) + \boldsymbol{\xi}_2(k,\mathbf{x}).\end{aligned} \tag{57}$$

For the disturbance item $\boldsymbol{\xi}_2(k,\mathbf{x})$, it can be divided into the dc component ($\boldsymbol{\xi}_{2e}(k)$) and the harmonic components ($\boldsymbol{\xi}_{2\,u}(k)$). The dc component is closely related to the angular speed and it varies slowly. The harmonic components are caused by the harmonics of $\mathbf{x}(k)$ and $\mathbf{u}_{\gamma\delta}(k)$. The state of the switching function can be obtained by solving the above difference equation as

$$\begin{aligned}\mathbf{s}(k+1) = {} & \mathbf{Q}^k\mathbf{s}(1) \\ & + \sum_{j=0}^{k-1}\mathbf{Q}^j(\boldsymbol{\xi}_{2e}(k) + \hat{\mathbf{e}}_{\gamma\delta}(k-j) - \mathbf{e}_{\gamma\delta}(k-j)) \\ & + \sum_{j=0}^{k-1}\mathbf{Q}^j(\boldsymbol{\xi}_{2\,u}(k) + \mathbf{d}(k-j) - \hat{\mathbf{d}}(k-j)).\end{aligned} \tag{58}$$

Therefore, the stability of the proposed observer with parameter variation can be also guaranteed, but the estimation error occurs inevitably.

VII. Validation and Analysis

Some validations are established to verify the effectiveness of the proposed sliding-mode observer by simulations performed in MATLAB/Simulink and experiments. The parameters of the system are shown in Table II and the parameters of the proposed method are shown in Table III. All the data of the experiments are sent to the host PC by the Ethernet module in the control board. The experimental setup is shown in Fig. 8.

A fan is installed on the shaft of the test motor as a load and thus the load torque is approximately proportional to the square of the motor speed, as shown in Table IV.

TABLE II
PARAMETERS OF THE EXPERIMENTAL PLANT

Symbol	Parameter	Value
R	winding resistance	0.023Ω
L_1	inductance at the inverter side	54μH
L_{2o}	inductance at the machine side	27.5μH
L_s	inductance of the machine	24μH
C_1	ac-side capacitor of LCL filter	31.48μF
f_{res}	resonant frequency	5525Hz
U_{DC}	DC bus voltage	65V
$poles$	poles of the machine	2
f_s	switching frequency	20kHz
T	sampling period	50μs
n_N	the rated speed	100kr/min
ψ_m	flux of the PM	0.0012Wb

TABLE III
PARAMETERS OF THE PROPOSED METHOD

Symbol	Value
Q_1, Q_2	0.5
p_L	$[0.7\ \ 0.8]^T$
p_u	$[0.5\ \ 0.6\ \ 0.6\ \ 0.65]^T$
φ	0.12
Ω	188.5 rad/s

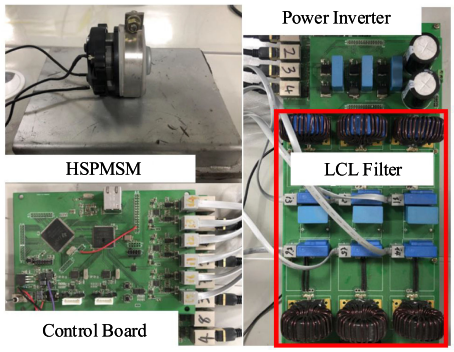

Fig. 8. Schematic diagram of the experimental setup.

TABLE IV
q-AXIS CURRENT WITH DIFFERENT SPEEDS

Speed	q-axis current
30 kr/min	4A
60 kr/min	10A
100 kr/min	30A

A. Rotor Position Estimation Performance

Fig. 9 shows the experimental results of the rotor estimation performance with the proposed method at 30, 60, and 100 kr/min. The installation of the position sensors (encoder or resolver) is difficult for a HSPMSM with rated speed up to 100 kr/min. In order to evaluate the position estimation accuracy, a current-injection validation is implemented, as shown in Fig. 11. During the injection, the speed controller still works to maintain the speed. Because of the same load, the q-axis current has to be same and there is

$$i^1_{2\delta}\cos\tilde{\theta}_e = i^2_{2\delta}\cos\tilde{\theta}_e + i^2_{2\gamma}\sin\tilde{\theta}_e \tag{59}$$

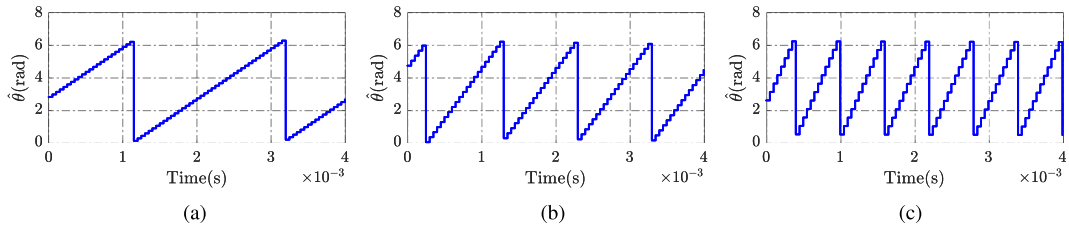

Fig. 9. Experimental results: the rotor estimation performance with the proposed method at 30, 60, and 100 kr/min. (a) At 30 kr/min. (b) At 60 kr/min. (c) At 100 kr/min.

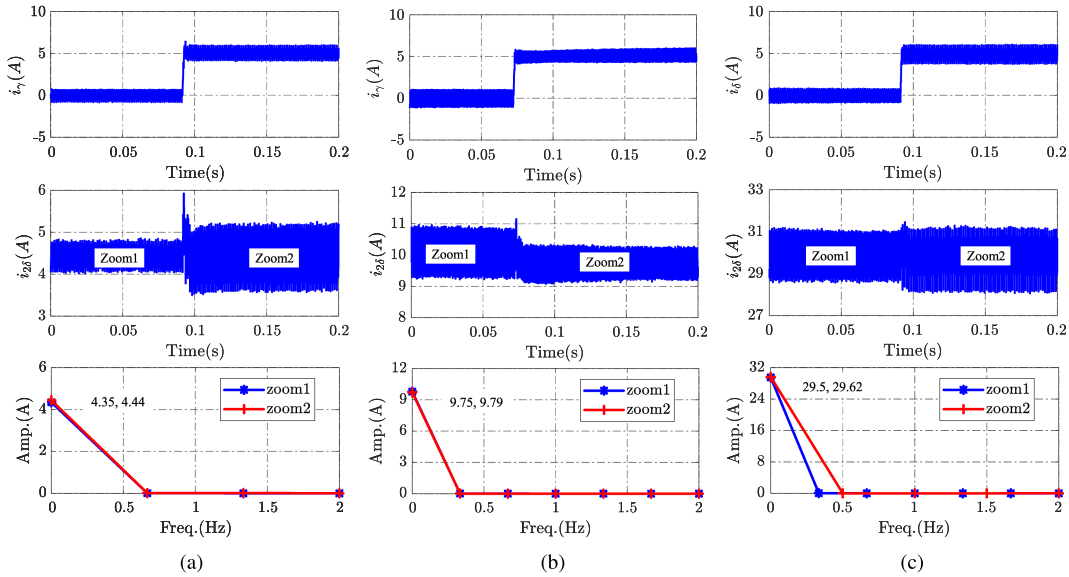

Fig. 10. Experimental results: the rotor estimation accuracy test with the current injection ($+5\ A$) method at 30, 60, and 100 kr/min. (a) At 30 kr/min. (b) At 60 kr/min. (c) At 100 kr/min.

where the $i^1_{2\delta}$ is the δ-axis motor current value with the $i_{2\gamma}=0$ and the $i^2_{2\delta}$ is the the δ-axis motor current value with a positive $i^2_{2\gamma}$ injected. Therefore, the estimation error can be calculated as

$$\tilde{\theta}_e = \text{atan}\left(\frac{i^1_{2\delta} - i^2_{2\delta}}{i^2_{2\gamma}}\right). \tag{60}$$

Fig. 10 shows the $i_{2\delta}$ performance when a +5 A is injected into the γ axis at 30, 60, and 100 kr/min, respectively. As well known, only the direct component of the q-axis current produces torque. To illustrate the variation of $i_{2\delta}$ clearly, the FFT analysis before the injection and after the injection are also provided. In Fig. 10(a), with the injected γ-axis current, the $i_{2\delta}$ has a small increase from 4.35 to 4.44 A. Based on (60), the estimation error can be calculated as 0.018 rd (i.e., 1.03°). As shown in Fig. 10(b) and (c), the position estimation error at 60 and 100 kr/min can calculated as 0.008 and 0.024 rd (i.e., 0.46° and 1.375°), respectively. Therefore, the position estimation of the proposed method is with high accuracy, even at high speed, which is beneficial from the fully discretized model.

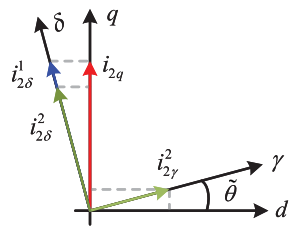

Fig. 11. Current vector diagram with current injection.

B. Chattering Suppression and Speed Estimation Performance

In order to compare the chattering suppression ability of the proposed method with the reaching law in [17], the attraction function $\mathbf{w}_{\gamma\delta}$ is designed as

$$\mathbf{w}_{\gamma\delta}(k) = (-\mathbf{G}_s + \mathbf{Q})\mathbf{s}(k) + \hat{d}(k) \tag{61}$$

and

$$\hat{d}(k) = \hat{d}(k-1) + \mathbf{s}(k) - \mathbf{Q}\mathbf{s}(k). \tag{62}$$

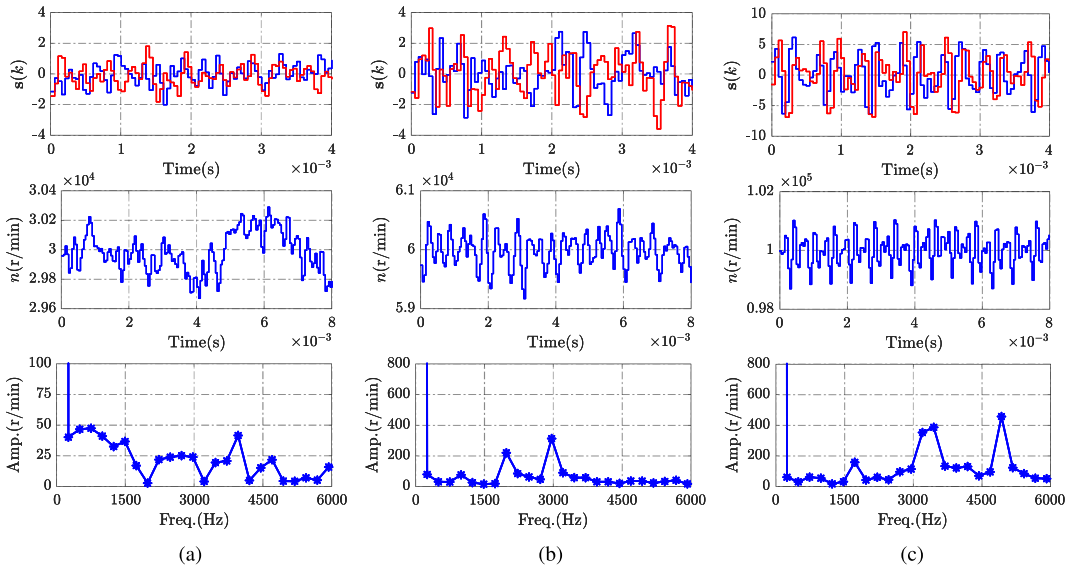

Fig. 12. Experimental results: the chattering and the speed estimation performance with the reaching law (61) at 30, 60, and 100 kr/min. (a) At 30 kr/min. (b) At 60 kr/min. (c) At 100 kr/min.

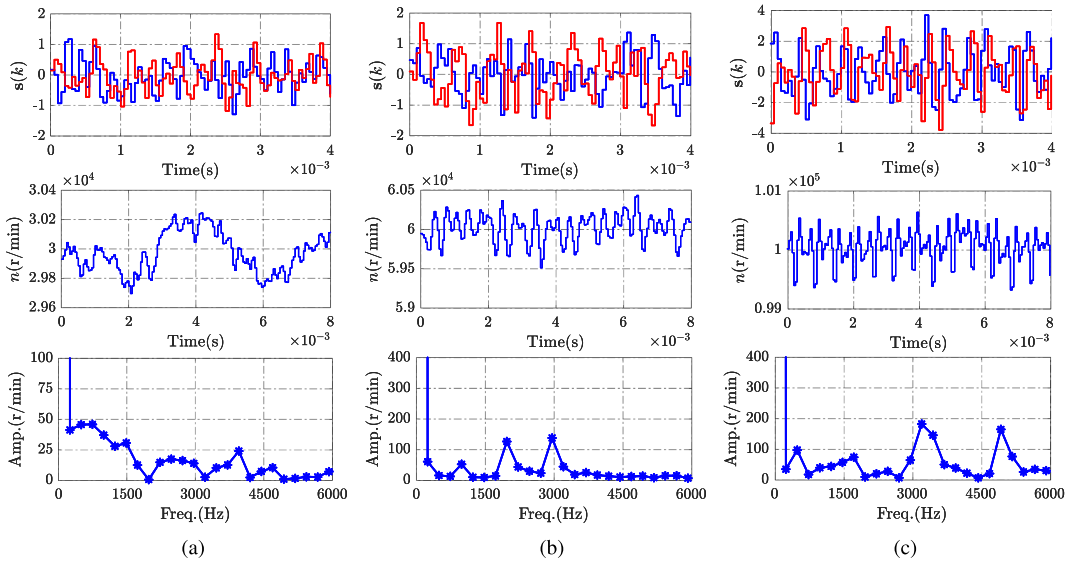

Fig. 13. Experimental results: the chattering and the speed estimation performance with the proposed reaching law at 30, 60, and 100 kr/min. (a) At 30 kr/min. (b) At 60 kr/min. (c) At 100 kr/min.

Therefore, a low-pass filter is used to extract the back EMF as

$$\hat{\mathbf{e}}_{\gamma\delta}(z) = \frac{k}{z-1+k}\mathbf{w}_{\gamma\delta}(z) \tag{63}$$

where the k is the same as the EMF adaption gain in the proposed method. In this way, the attenuation of the low-pass filter in both methods is equivalent.

Fig. 12 shows the experimental results of the speed estimation performance with the reaching law (61) at 30, 60, and 100 kr/min. In Fig. 12(a), at 30 kr/min, since the high ratio of sampling/fundamental frequency, the chattering $\mathbf{s}(k)$ is relatively small and thus the speed estimation ripple is within $\pm$200 r/min. With the speed up, the speed estimation ripple is increased with the enlarged chattering. The speed estimation ripple can be $\pm$600 r/min at 60 kr/min and $\pm$1100 r/min at 100 kr/min, as shown in Fig. 12(b) and (c), respectively. Besides, as the FFT analysis illustrated, the speed estimation ripple is mainly located around $2f_e$ (2000 Hz at 60 kr/min and 3300 Hz at 100 kr/min) and $3f_e$ (3000 Hz at 60 kr/min and 5000 Hz at 100 kr/min), which result from the ADC scaling error and the PWM harmonic.

Fig. 13 shows the experimental results of the speed estimation performance with the proposed method at 30, 60, and 100 kr/min. At 30 kr/min, as shown in Fig. 13(a), because of the high sampling/fundamental frequency, the chattering $\mathbf{s}(k)$ is relatively small and thus the speed estimation ripple is within

TABLE V
SPEED ESTIMATION RIPPLE COMPARISON

Speed	Reaching law (61)	Proposed Method
30 kr/min	±200 r/min	±200 r/min
60 kr/min	±600 r/min	±350 r/min
100 kr/min	±1100 r/min	±600 r/min

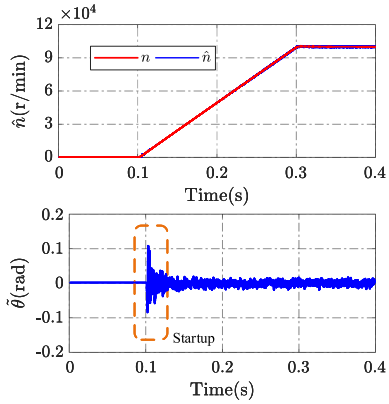

Fig. 14. Simulation results: the rotor estimation performance when the speed is driven from 0 to 100 kr/min.

±200 r/min, which is the same as Fig. 12(a). The speed estimation ripple can be ±350 r/min at 60 kr/min and ±600 r/min at 100 kr/min, as shown in Fig. 13(b) and (c), respectively. Besides, as the FFT analysis demonstrated, it can be easily observed that the speed estimation ripple, mainly located around $2f_e$ and $3f_e$, is well reduced compared with the reaching law (61).

The speed estimation ripple comparison at 30, 60, and 100 kr/min is shown in Table V.

C. Speed Accelerating

1) Simulation Results: Fig. 14 shows the simulation results of the rotor estimation performance when the speed is driven from 0 to 100 kr/min. It can be observed that the position estimation error is still less than 0.02 rd during the speed accelerating process.

2) Experimental Results: In Fig. 15, the tested HSPMSM is driven form 0 up to 100 kr/min. Because of the position sensorless drive, first, the tested motor will be driven with the external forced synchronous angle and the torque-controlled mode is implemented. After the back EMF is adequately detected, the position sensorless drive and the speed controller work. Besides, the rotor position estimation at startup, as shown in Fig. 16.

Fig. 17 shows the experimental results of the phase A current waveforms at 60 and 100 kr/min. Clearly, the motor current is well filtered with the attenuation of the *LCL* filter. Fig. 18 shows the experimental results of phase A capacitor voltage waveform and its FFT analysis at 100 kr/min. From the observation, there exist the harmonic components located at $2f_e$ and $3f_e$, which result from the ADC scaling error and the PWM harmonic, respectively.

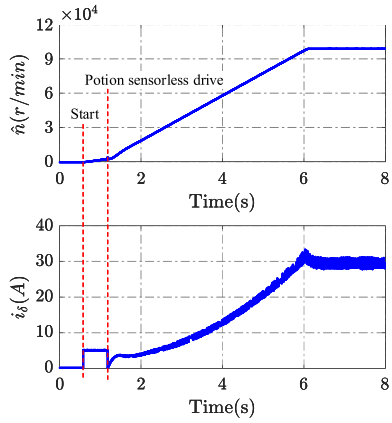

Fig. 15. Experimental results: position sensorless drive performance when the speed is driven from 0 to 100 kr/min.

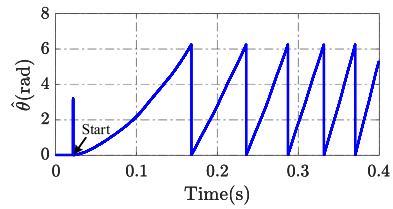

Fig. 16. Experimental results: the position estimation performance at startup.

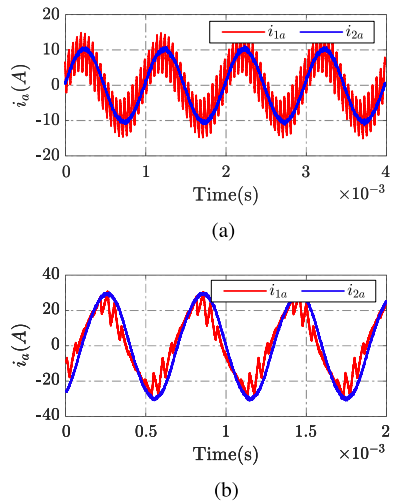

Fig. 17. Experimental results: phase A current waveforms at 60 and 100 kr/min. (a) Phase A current at 60 kr/min. (b) Phase A current at 100 kr/min.

D. Torque Changing Performance and Speed Reversal

1) Simulation Results: Fig. 19 shows the simulation results of the rotor position estimation performance with torque change from 10 to 15 A. At 0.05 s, the $i_{2\delta}$ has a stepping increase and the position estimation error is still within 0.1 rd.

2) Experimental Results: Fig. 20 shows the experimental results of $i_{2\delta}$ and rotor estimation performance with torque change from 10 to 15 A. It can be observed that the stepping

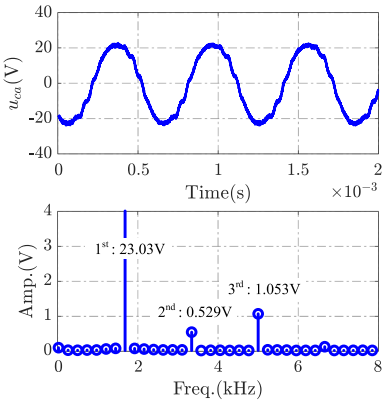

Fig. 18. Experimental results: phase A capacitor voltage waveform and its FFT analysis at 100 kr/min.

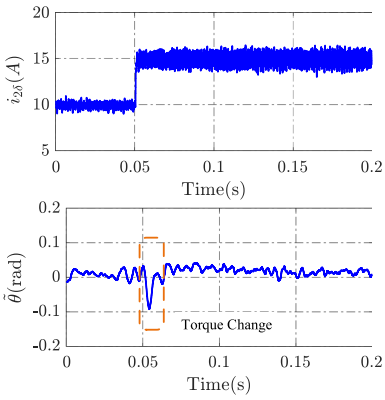

Fig. 19. Simulation results: rotor position estimation performance with torque change from 10 to 15 A.

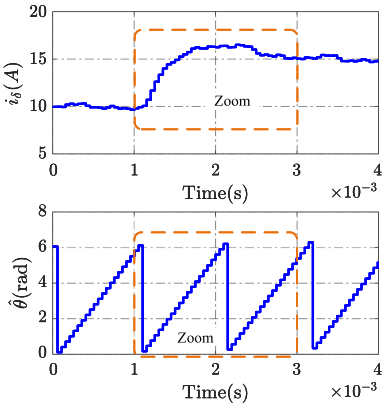

Fig. 20. Experimental results: i_δ and rotor estimation performance with torque change from 10 to 15 A.

increasing $i_{2\delta}$ has small effects on the rotor position estimation. Fig. 21 shows the estimated speed with the torque current change. Because the motor load is a fan, when the torque current is increased, the motor will be accelerated and the ideal speed curve is demonstrated as the red line in Fig. 21. Therefore, the maximum speed estimation error is around 150 r/min during the

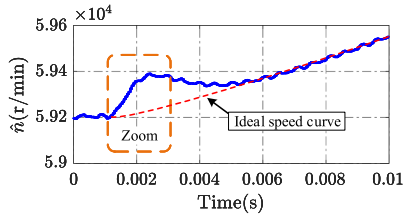

Fig. 21. Experimental results: speed estimation performance with torque current from 10 to 15 A.

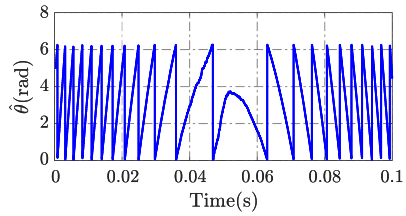

Fig. 22. Experimental results: the rotor estimation performance with speed reversal.

torque changing process. Fig. 22 shows the experimental results of the rotor estimation performance with speed reversal.

E. Robustness Against Parameter Variation

To validate the enhanced robustness against the parameter variation, a comparison with a linear observer is established. The discrete-time state-space model in $\alpha\beta$ stationary frame is expressed as

$$\begin{cases} \begin{bmatrix} \mathbf{x}_1(k+1) \\ \mathbf{x}_2(k+1) \end{bmatrix} = \begin{bmatrix} \mathbf{G}_{s11} & \mathbf{G}_{s12} \\ \mathbf{G}_{s21} & \mathbf{G}_{s22} \end{bmatrix} \begin{bmatrix} \mathbf{x}_1(k) \\ \mathbf{x}_2(k) \end{bmatrix} \\ \quad + \begin{bmatrix} \mathbf{H}_{s11} \\ \mathbf{H}_{s22} \end{bmatrix} \mathbf{u}_s(k) \\ \mathbf{y}_s(k) = \mathbf{x}_1(k) \end{cases} \tag{64}$$

where

$$\mathbf{x}_1(k) = \left[\mathbf{i}_{1\,s}(k)\ \mathbf{i}_{2\,s}(k) \right]^T$$
$$\mathbf{x}_2(k) = \left[\mathbf{u}_{cs}(k)\ \mathbf{e}_s(k) \right]^T.$$

Based on the discrete-time model, the linear reduced-order observer in $\alpha\beta$ frame is designed as

$$\begin{cases} \hat{\mathbf{x}}_2(k) = \mathbf{z}(k) + \mathbf{L}\mathbf{y}_s(k) \\ \mathbf{z}(k+1) = \underbrace{(\mathbf{G}_{s22} - \mathbf{L}_s\mathbf{G}_{s12})}_{\Theta} \hat{\mathbf{x}}_2(k) \\ \quad + (\mathbf{G}_{s21} - \mathbf{L}\mathbf{G}_{s11})\,\mathbf{y}_s(k) \\ \quad + (\mathbf{H}_{s22} - \mathbf{L}_s\mathbf{H}_{s11})\,\mathbf{u}_s(k) \end{cases} \tag{65}$$

with

$$\hat{\mathbf{x}}_2(k) = \left[\hat{\mathbf{u}}_{cs}(k)\ \hat{\mathbf{e}}_s(k) \right]^T$$

where the $\hat{}$ denotes the estimated value and the $\mathbf{L}_s$ is the gain matrix of the reduced-order observer. The stability and the convergence speed of the observer depends on the eigenvalues of the matrix Θ.

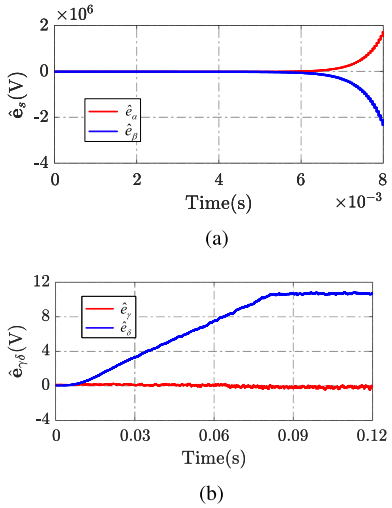

Fig. 23. Robustness comparison between the proposed sliding-mode observer and the linear observer with the 200% real ac-side capacitor adopted in the observer. (a) Linear observer. (b) Proposed sliding-mode observer.

TABLE VI
EXECUTION TIME OF PROPOSED OBSERVER AND PLL

	Execution Time (System Cycle)
Current Prediction	489
Reaching Law Calculation	268
PLL	28
Sum	785

Without loss of generality, the variation of the ac-side capacitor is implemented. Fig. 23 shows the robustness comparison between the proposed sliding-mode observer and the linear observer with the 200% real ac-side capacitor adopted in the observer. The poles of the linear observer is selected as $[0.4, 0.4, 0.5, 0.5]^T$. In Fig. 23(a), the linear observer is unstable while the proposed method still works well in Fig. 23(b). Therefore, from the aspect of this point, the proposed sliding-mode observer has more robustness compared with the linear observer.

F. Execution Time

The microprocessor adopted in the control board is TMS320F28335 provided by *Texas Instruments* and the system clock is 150 MHz. The execution time is obtained by a timer in parallel. The result is demonstrated in Table VI. It is worth noting that the coefficient matrices of the proposed observer are calculated offline and given as a lookup table in the microprocessor. The execution time of the proposed parameter estimation is approximately 785 system cycles (5.23 μs for a 150 MHz microprocessor). Therefore, it is also acceptable even implemented in low-system-clock applications.

VIII. CONCLUSION

This article proposes a sliding-mode position estimation method for HSPMSMs with *LCL* filter.

1) A sliding-mode back EMF observer is designed to enhance robustness against the parameter variation compared with the linear observer. The solid design steps of the proposed method are provided.
2) An optimized reaching law with the EMF adaption law and periodic-disturbance suppression method is proposed to achieve reduced chattering and speed estimation ripple compared with the reaching law in [17].

Finally, the effectiveness of the proposed sliding-mode observer is validated by the simulation and experimental results.

REFERENCES

[1] D. Gerada, A. Mebarki, N. L. Brown, C. Gerada, A. Cavagnino, and A. Boglietti, "High-speed electrical machines: Technologies, trends, and developments," *IEEE Trans. Ind. Electron.*, vol. 61, no. 6, pp. 2946–2959, Jun. 2014.
[2] K. Yamazaki and A. Abe, "Loss analysis of interior permanent magnet motors considering carrier harmonics and magnet eddy currents using 3-D FEM," in *Proc. IEEE Int. Electr. Mach. Drives Conf.*, May 2007, vol. 2, pp. 904–909.
[3] W. Wu, Y. Liu, Y. He, H. S. H. Chung, M. Liserre, and F. Blaabjerg, "Damping methods for resonances caused by LCL-filter-based current-controlled grid-tied power inverters: An overview," *IEEE Trans. Ind. Electron.*, vol. 64, no. 9, pp. 7402–7413, Sep. 2017.
[4] S. Chi, Z. Zhang, and L. Xu, "Sliding-mode sensorless control of direct-drive PM synchronous motors for washing machine applications," *IEEE Trans. Ind. Appl.*, vol. 45, no. 2, pp. 582–590, Mar. 2009.
[5] H. Kim, M. C. Harke, and R. D. Lorenz, "Sensorless control of interior permanent magnet machine drives with zero-phase-lag position estimation," *IEEE Trans. Ind. Appl.*, vol. 39, no. 6, pp. 1726–1733, Nov./Dec. 2003.
[6] S. Morimoto, K. Kawamoto, M. Sanada, and Y. Takeda, "Sensorless control strategy for salient-pole PMSM based on extended EMF in rotating reference frame," *IEEE Trans. Ind. Appl.*, vol. 38, no. 4, pp. 1054–1061, Jul. 2002.
[7] S. C. Yang and G. R. Chen, "High-speed position-sensorless drive of permanent-magnet machine using discrete-time EMF estimation," *IEEE Trans. Ind. Electron.*, vol. 64, no. 6, pp. 4444–4453, Jun. 2017.
[8] T. Tuovinen, H. A. A. Awan, S. E. Saarakkala, and M. Hinkkanen, "Discrete-time observer design for sensorless synchronous motor drives," in *Proc. IEEE Energy Convers. Congr. Expo.*, 2015, pp. 867–874.
[9] T. Bernardes, V. F. Montagner, H. A. Gründling, and H. Pinheiro, "Discrete-time sliding mode observer for sensorless vector control of permanent magnet synchronous machine," *IEEE Trans. Ind. Electron.*, vol. 61, no. 4, pp. 1679–1691, Apr. 2014.
[10] J. Kukkola and M. Hinkkanen, "Observer-based state-space current control for a three-phase grid-connected converter equipped with an LCL filter," *IEEE Trans. Ind. Appl.*, vol. 50, no. 4, pp. 2700–2709, Jul. 2014.
[11] B. Wang, Y. Xu, Z. Shen, J. Zou, C. Li, and H. Liu, "Current control of grid-connected inverter with LCL filter based on extended-state observer estimations using single sensor and achieving improved robust observation dynamics," *IEEE Trans. Ind. Electron.*, vol. 64, no. 7, pp. 5428–5439, Jul. 2017.
[12] C.-C. Hsu, S.-C. Yang, and J.-Y. Chen, "Implementation of low inductance permanent magnet machine drive with LC filter for field oriented control," in *Proc. IEEE Energy Convers. Congr. Expo.*, 2019, pp. 6140–6146.
[13] J. Kukkola, M. Hinkkanen, and K. Zenger, "Observer-based state-space current controller for a grid converter equipped with an LCL filter: Analytical method for direct discrete-time design," *IEEE Trans. Ind. Appl.*, vol. 51, no. 5, pp. 4079–4090, Sep. 2015.
[14] M. Su *et al.*, "Single-sensor control of LCL-filtered grid-connected inverters," *IEEE Access*, vol. 7, pp. 38481–38494, 2019.
[15] Y. Yao, Y. Huang, and F. Peng, "Position sensorless drive of high speed permanent magnet synchronous motor," in *Proc. IEEE Energy Convers. Congr. Expo.*, 2018, pp. 1733–1740.
[16] C. Edwards, *Sliding Mode Control : Theory and Applications*. Boca Raton, FL, USA: CRC Press, Aug. 1998.
[17] S. Qu, X. Xia, and J. Zhang, "Dynamics of discrete-time sliding-mode-control uncertain systems with a disturbance compensator," *IEEE Trans. Ind. Electron.*, vol. 61, no. 7, pp. 3502–3510, Jul. 2014.
[18] H. Ma, J. Wu, and Z. Xiong, "A novel exponential reaching law of discrete-time sliding-mode control," *IEEE Trans. Ind. Electron.*, vol. 64, no. 5, pp. 3840–3850, May 2017.

[19] D.-W. Chung and S.-K. Sul, "Analysis and compensation of current measurement error in vector-controlled AC motor drives," *IEEE Trans. Ind. Appl.*, vol. 34, no. 2, pp. 340–345, Mar. 1998.
[20] S. G. Parker, B. P. McGrath, and D. G. Holmes, "Regions of active damping control for LCL filters," *IEEE Trans. Ind. Appl.*, vol. 50, no. 1, pp. 424–432, Jan. 2014.
[21] D. G. Holmes and T. A. Lipo, *Pulse Width Modulation for Power Converters: Principles and Practice*. Hoboken, NJ, USA: Wiley, Oct. 2003.
[22] D. Holmes and B. McGrath, "Opportunities for harmonic cancellation with carrier-based PWM for a two-level and multilevel cascaded inverters," *IEEE Trans. Ind. Appl., vol.* 37, no. 2, pp. 574–582, Mar./Apr. 2001.
[23] F. Peng, J. Ye, A. Emadi, and Y. Huang, "Position sensorless control of switched reluctance motor drives based on numerical method," *IEEE Trans. Ind. Appl.*, vol. 53, no. 3, pp. 2159–2168, May 2017.

Yu Yao (Student Member, IEEE) received the B.S. degree in electrical engineering in 2016 from Southeast University, Nanjing, China, where he is currently working toward the Dr. Eng. in electric machines and control with the School of Electrical Engineering.

His main research interests include the design of the power inverter, the current regulator design, the position sensorless drive for the high-speed PSMSM, and active damping methods for the high-speed drive system with *LCL* output filter.

Yunkai Huang received the M.Sc. and Ph.D. degrees in electrical engineering from the Southeast University, Nanjing, China, in 2001 and 2007, respectively.

He is currently a Professor with the School of Electrical Engineering, Southeast University. His research interests include design and control of PM machine and high speed machine, applications in domestic appliances, electric vehicles, railway traction, all-electric ships, more-electric aircraft, and wind power generation systems.

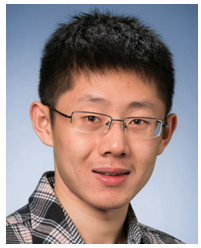

Fei Peng (Member, IEEE) received the B.S. and M.S. degrees in electrical engineering from Southeast University, Nanjing, China, in 2010 and 2012, respectively, and the Ph.D. degree in electrical and computer engineering from McMaster University, Hamilton, ON, Canada, in 2016.

After that he was a Postdoctoral Fellow with the McMaster Institute for Automotive Research and Technology, McMaster University. Since December 2016, he has been an Assistant Professor with the School of Electrical Engineering, Southeast University. His research interests include optimal design and control of power converters, modeling, and digital control of motor drives.

Jianning Dong (Member, IEEE) received the B.S. and Ph.D. degrees in electrical engineering from Southeast University, Nanjing, China, in 2010 and 2015, respectively.

Since 2016, he has been an Assistant Professor with the Delft University of Technology, Delft, The Netherlands. Before joining TU Delft, he was a Postdoctoral Researcher with McMaster Automotive Resource Centre, McMaster University, Hamilton, ON, Canada. His main research interests include design, modeling, and control of electromechanical systems.